Dynamic viability of the 2016 Mw 7.8 Kaikōura earthquake cascade on weak crustal faults

Thomas Ulrich*[1], Alice-Agnes Gabriel[1], Jean-Paul Ampuero[2,3] and Wenbin Xu[4]

* ulrich@geophysik.uni-muenchen.de

1 Department of Earth and Environmental Sciences, Ludwig-Maximilians-Universität München, Germany

2 Université Côte d'Azur, IRD, CNRS, Observatoire de la Côte d'Azur, Géoazur, France

3 Seismological Laboratory, California Institute of Technology, USA

4 Department of Land Surveying and Geo-Informatics, Hong Kong Polytechnic University, Hong Kong, China

Abstract

We present a dynamic rupture model of the 2016 Mw 7.8 Kaikōura earthquake to unravel the event's riddles in a physics-based manner and provide insights on the mechanical viability of competing hypotheses proposed to explain them. Our model reproduces key characteristics of the event and constraints puzzling features inferred from high-quality observations including a large gap separating surface rupture traces, the possibility of significant slip on the subduction interface, the non-rupture of the Hope fault, and slow apparent rupture speed. We show that the observed rupture cascade is dynamically consistent with regional stress estimates and a crustal fault network geometry inferred from seismic and geodetic data. We propose that the complex fault system operates at low apparent friction thanks to the combined effects of overpressurized fluids, low dynamic friction and stress concentrations induced by deep fault creep.

Introduction

The Mw 7.8 Kaikōura earthquake struck New Zealand's South Island on November 14, 2016. This event, considered the most complex rupture observed to date, caused surface rupture of at least 21 segments of the Marlborough fault system, some of them previously unknown. Puzzling features inferred from high-quality observations include a large gap separating surface rupture traces, the possibility of significant slip on the subduction interface, and slow apparent rupture speed. Here we develop a dynamic rupture model to unravel the event's riddles in a physics-based manner. Our model reproduces key characteristics of the event and provides insights on the mechanical viability of competing hypotheses proposed to explain them. We show that the observed rupture cascade, involving strike and thrust faulting, is dynamically consistent with regional stress estimates and a crustal fault network geometry inferred from seismic and geodetic data. The rupture propagation requires a linking low-dipping shallow thrust fault, but not slip on an underlying megathrust. The apparent rupture slowness is explained by a zigzagged propagation path and rupture delays at the transitions between faults. The complex fault system operates at low apparent friction thanks to the combined effects of overpressurized fluids, low dynamic friction and stress concentrations induced by deep fault creep. Our results associate the non-rupture of the Hope fault, one of the fundamental riddles of the event, with unfavourable dynamic stresses on the restraining step-over formed by the Conway-Charwell and Hope faults.

Studies of the Kaikōura earthquake based on geological, geodetic, tsunami and seismic data reveal puzzling features as well as observational difficulties. An apparent gap of 15-20 km in surface rupture between known faults (Hamling et al., 2017) may suggest a rupture jump over an unexpectedly large distance or the presence of deep fault segments connecting surface rupturing faults. Rupture duration is long, more than twice the average duration of past earthquakes of same magnitude (Duputel and Rivera, 2017). Finite-fault source inversion models inferred from strong motion and other data (Bradley et al. (2017), Holden et al. (2017) and Wang et al. (2018)) present unconventional kinematic features, such as unusually large delays between segments (Bradley et al., 2017) or strong scatter in the distribution of rupture time (Wang et al., 2018). The rupture may include simultaneous slip on the Hikurangi subduction interface (Wang et al., 2018) and several segments slipping more than once (Holden et al., 2017). Teleseismic back-projection studies (Hollingsworth et al. (2017), Xu et al. (2018), Zhang et al. (2017)) agree on general earthquake characteristics (e.g. an overall SW-NE propagation direction) but not on the space-time evolution of the rupture.

Competing views of the role played by the Hikurangi subduction interface during the Kaikōura earthquake have emerged from previous studies. Whereas far-field teleseismic and some tsunami data inferences require thrust faulting on a low dipping fault, interpreted as the subduction interface beneath the Upper Kowhai and Jordan Thrust faults (Bai et al., 2017, Hollingsworth et al., 2017, Duputel and Rivera, 2017, Wang et al., 2018), analysis of strong motion, aftershocks, geodetic and coastal deformation observations find little or no contribution of the subduction interface (Holden et al., 2017, Clark et al., 2017, Cesca et al., 2017, Xu et al., 2018). The geometry of the Hikurangi megathrust is not well constrained in its Southern end (Williams et al., 2013): dipping angles assumed in previous studies range from 12 to 25 degrees (Hamling et al., 2017; Wang et al., 2018). Large-scale ground-deformations have then been explained by either slip on the subduction interface (e.g. Hamling et al., 2017, Wang et al., 2018) or by crustal models featuring listric fault geometries (Xu et al., 2018) or shallow thrust faults (Clark et al., 2017).

Incorporating the requirement that the rupture should be dynamically viable can help constrain the unexpected features and competing views of this event. Analyses of static Coulomb failure stress changes during rupture provides some mechanical insight on the rupture sequence (Hamling et al. (2017), Xu et al. (2018)), but do not account for dynamic stress changes, which are an important factor in multi-fault ruptures (e.g., Bai and Ampuero, 2017). Dynamic rupture simulations provide physically self-consistent earthquake source descriptions, and have been used to study fundamental aspects of earthquake physics (e.g. Gabriel et al., 2012, Shi and Day, 2013), to assess earthquake hazard (e.g., Aochi and Ulrich, 2015) and to understand previous earthquakes (e.g. Olsen et al. (1997), Ma et al. (2008)). The dynamic rupture modelling presented here provides physical arguments to discriminate between competing models of the fault system geometry and faulting mechanisms.

Mature plate boundary faults are, in general, apparently weak (Zoback et al., 1987; Behr and Platt, 2014; England, 2018), a feature that is required also by long-term geodynamic processes (e.g. Duarte et al., 2015; Osei Tutu et al., 2018) but that seems incompatible with the high static frictional strength of rocks (Byerlee, 1978). These two observations can be reconciled by considering dynamic weakening, which allows faults to operate at low average shear stress (Noda et al., 2009). However, low background stresses are generally unfavourable for rupture cascading across a network of faults. For instance, rupture jumps across fault stepovers are hindered by low initial stresses (Bai and Ampuero, 2017). This is one reason why finding a viable dynamic rupture model is non-trivial. The modelled fault system presented here features a low apparent friction while being overall favourably oriented with respect to the background stress. We demonstrate that fault weakness is compatible with a multi-fault cascading rupture. Our models suggest that such a weak-fault state is actually required to reproduce the Kaikoura cascade (see method sec. A7).

Our dynamic model of the Kaikōura earthquake is tightly determined by integrating knowledge and data spanning a broad range of scales. It combines an unprecedented degree of realism, including a modern laboratory-based friction law, off-fault inelasticity, seismological estimates of regional stress, a realistic fault network geometry model, a 3D subsurface velocity model and high-resolution topography and bathymetry. High resolution 3D modeling is enabled by the SeisSol software package that couples seismic wave propagation with frictional fault failure and off-fault inelasticity, and is optimized for high-performance computing. The resulting dynamic model of the Kaikōura earthquake sheds light on the physical mechanisms of cascading ruptures in complex fault systems.

1. Model

1.1 Fault geometry

We construct a model of the non-planar, intersecting network of crustal faults (fig. 1) by combining constraints from previous observational studies and from dynamic rupture modeling experiments. Fault geometries and orientations have been constrained by geological and geodetic data (e.g. Litchfield et al., 2014, Nicol et al., 2018, Xu et al., 2018). Our starting point is a smoothed version of the fault network geometry “model III” inferred from field and remote sensing data by Xu et al. (2018). It comprises three strike-slip faults: Humps and Stone Jug faults and a long segment with listric geometry (flattening at depth) resembling jointly the Hope-Upper Kowhai-Jordan Thrust, Kekerengu and Needles faults; and four thrust faults: Conwell-Charwell, Hundalee, Point Kean and Papatea faults. The model does not include the subduction interface but is sufficient to explain the observed static ground deformations in the near-field and far-field.

We extend this simplified model to capture the complexity of the southern part of the fault network. The western tip of the Humps segment is slightly rotated (azimuth direction from WSW to W) in our model. The improved agreement with the mapped surface rupture enables spontaneous termination of the westward rupture front. We substitute the Conway-Charwell fault zone by the distinct Leader and Conway-Charwell faults (Nicol et al., 2018). The geometry of the Leader fault is similar to the Conway-Charwell fault zone of Xu et al. (2018)'s model, however the former is increasingly steeper to the North. Surface rupture mapping suggests a segmentation of the Leader fault in at least two segments (Nicol et al., 2018). Yet the continuity of the inferred ground-deformations in that region (Nicol et al., 2018) suggests a unified segment. Dynamic rupture experiments accounting for a large step-over within the Leader fault also suggest that a segmented geometry is not viable. The Conway-Charwell fault steps over the Leader fault. It runs roughly parallel to the Hope fault to the North. The Southernmost part of the long listric segment of Xu et al. (2018)'s geometry, representing the Hope fault, is replaced here by the Hope fault geometry proposed by Hamling et al. (2017), which is more consistent with the mapped fault trace and inferred dip angle (Litchfield et al., 2014). The 60° dipping Stone Jug fault of Xu et al. (2018) is replaced by a steeper fault, as suggested by Nicol et al. (2018). The Hundalee segment is shortened at its extremities, to limit its slip extent according to Xu et al. (2018)'s inversion results.

Based on experimental dynamic rupture simulations, we remove the Upper Kowhai fault. Instead, we postulate that the previously unknown Point Kean fault (Clark et al., 2017) acted as a crucial link between the Hundalee fault and the Northern faults. The Upper Kowhai fault is well oriented relative to the regional stress and, when included, experiences considerable slip in contradiction with observations. Although geodetic data suggest a moderate amount of slip on this fault at depth (Hamling et al., 2017; Xu et al., 2018), we hypothesize that such slip is not crucial for the continuation of the main rupture process. This is supported by recent evidence suggesting the rupture propagated from the Papatea fault to the Jordan thrust (more details in sec. 2), rather than a Jordan thrust - Papatea fault sequence mediated by slip on the Upper Kowhai fault. Moreover, localized slip at depth on the Upper Kowhai fault would be difficult to reproduce without additional small scale features in the fault geometry or fault strength heterogeneities.

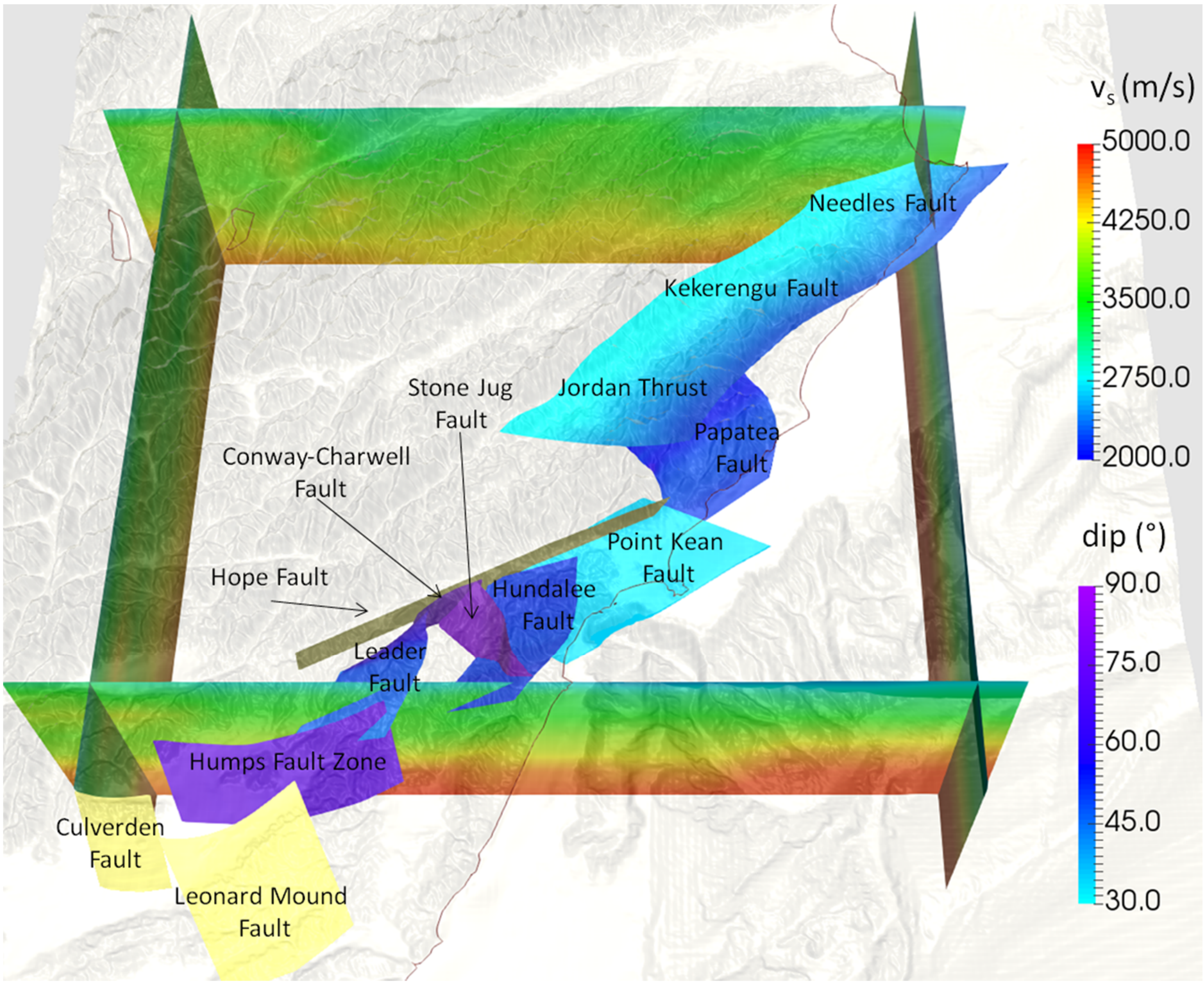

Figure 1: Fault network geometry prescribed for dynamic earthquake rupture modeling. Colors on fault surfaces indicate dipping angle (“dip”), highlighting the flattening with depth of the Jordan Thrust, Kekerengu and Needles faults. All segments dip westwards, except for the Humps Fault Zone. The Hope, Culverden and Leonard Mound faults, dipping respectively 70° toward NorthWest, 70° toward South and 50° toward SouthEast, are displayed in yellow. These faults do not rupture in our dynamic rupture model. Also shown

are the high-resolution topography and bathymetry (Mitchell et al., 2012) and S-wave speeds ("Vs") on four cross-sections of the 3D subsurface structure (Eberhart-Phillips et al., 2010) incorporated in the model.

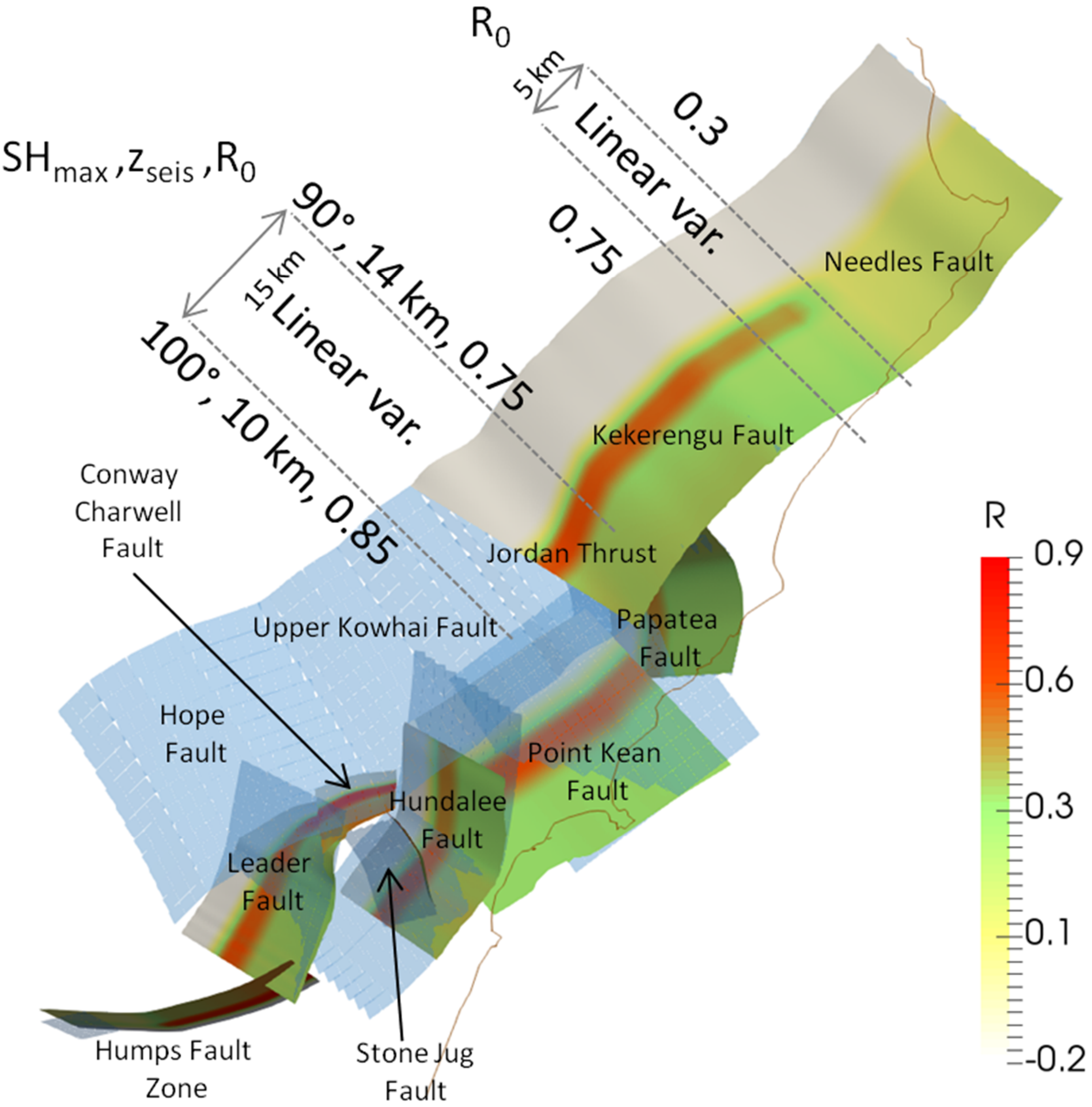

Figure 2: Adaptations made on the fault geometry of Xu et al. (2018) to develop a realistic dynamic rupture model. Changes made in the fault geometry are highlighted by plotting the final geometry over the fault geometry of Xu et al. (2018), shown in transparent blue. The distribution of initial fault stress ratio R (eq. 1) along the fault network is also shown. The spatial distributions of parameters defining the stress (SH_{max}, R and z_{seis} defined in methods

section A6) are indicated. The magnitude of the initial stress loading is decreased in the Needle fault region to prevent large slip on this optimally oriented segment (such decrease is modeled by decreasing R_0 by 60% and suppressing the deep stress concentrations in that region).

1.2 Friction

We constrain our model parameters based on findings from laboratory to tectonic scale. Specifically, incorporating realistic levels of static and dynamic frictional resistance and stress drop is an important goal in our model design.

In our model, adopting a friction law with severe velocity- weakening friction law enables full cascading rupture and realistic amounts of slip, in contrast with simplified friction laws. We adopt a friction law featuring rapid weakening at high slip velocity (adapted from Dunham et al. (2011) as detailed in methods section A4) which reproduces the dramatic friction decrease observed in laboratory experiments at co-seismic slip rates (Di Toro et al., 2011). Comparing to results of our numerical experiments with linear slip-weakening friction (e.g. Andrews, 1976) on the same fault geometry, we find that strong velocity-weakening facilitates rupture cascading because it yields a smaller critical size to initiate self-sustained rupture by dynamic triggering.

1.3 Initial stresses

The stresses acting on natural faults and their strength are difficult to quantify. Although strength parameters are measured in laboratory friction experiments (Di Toro et al., 2011) and estimated from different types of observations (Copley, 2018), little consensus about the actual strength of faults exists (Hardebeck, 2015). We introduce new procedures to constrain the initial fault stress and relative strength. This systematic approach, detailed in methods section A6 and fig. S8, is constrained by observations and simple theoretical analysis, including seismo-tectonic observations, fault slip inversion models, deep aseismic creep, fault fluid pressurization, Mohr-Coulomb theory of frictional failure and strong dynamic weakening. In addition to static analysis, it requires only few trial simulations to ensure sustained rupture propagation. By efficiently reducing the non-uniqueness in dynamic modeling, this approach is superior to the common trial-and-error approach.

Our initial stress model is fully described by seven independent parameters (fig. S6): four parameters related to regional stress and seismogenic depth, which are directly constrained by observations, and three unknown parameters related to fluid pressure, background shear stress and the intensity of deep stress concentration. A stress state is fully defined by its principal stress magnitudes and orientations. The orientations of all components and the relative magnitude of the intermediate principal stress are constrained by seismological observations (Townend et al., 2012). In addition, the smallest and largest principal stress components are constrained by prescribing the prestress relatively to strength drop on optimally-oriented fault planes (Aochi and Madariaga, 2003). To determine the preferred initial stresses, we first ensure compatibility of the stress state with the prescribed fault geometry and the slip rakes inferred from static source inversion. In this purely static step, we determine optimal stress parameters, within their identified uncertainties, that maximize the ratio of shear to normal stress all over the fault and maximize the alignment between fault shear tractions and inferred slip (Xu et al., 2018). We then use a set of dynamic rupture simulations to determine the depth-dependent initial shear stress and fluid pressure that lead to subshear rupture and slip amounts consistent with previous source inversion studies. The resulting model incorporates over-pressurized fault zone fluids (Suppe, 2014; Sutherland et al., 2017; Uphoff et al., 2017) with a fluid pressure considerably higher than hydrostatic stress but well below lithostatic level (see method sec. A6).

A favourable stress orientation on all segments, including thrust and strike-slip faults, is promoted by an intermediate principal stress close to the maximum principal stress (Aochi et al., 2006) representing a transpressional regime. This configuration promotes thrust faulting on faults dipping at approximately 60 degrees and striking perpendicularly to the direction of maximum compression, which roughly corresponds with the thrust fault geometries of our model.

In our model, dynamic rupture cascading is facilitated by deep stress concentrations (fig. 2). The presence of stress concentrations at depth near the rheological transition between the locked and steady sliding portions of a fault is a known mathematical result of the theory of dislocations in elastic media (e.g. Kato, 2012, Bruhat and Segall, 2017). Such stress concentrations are also a typical result of interseismic stress calculations based on geodetically-derived coupling maps (Ader et al., 2012) or long-term slip rates (Mildon et al, 2017). Stress concentrations due to deep creep on the megathrust have been proposed to determine the rupture path independent of crustal fault characteristics (Lamb et al. 2018). Stress concentration is introduced in our model by two independent modulation functions (fig. S8).

Our initial stress model leads to low values of the initial shear to normal stress ratio over most of the seismogenic zone (the median value over the rupture area is 0.09, see fig. S9) in consistence with the apparent weakness of faults (Copley, 2018, methods section A7). Yet, most faults of our model are relatively well oriented with respect to the regional stress, and are therefore not weak in the classical sense. The classical Andersonian theory of faulting may be challenged in transpressional tectonic stress regimes resulting in non-unique faulting mechanisms. In the framework of dynamic rupture modeling, faults can be stressed well below failure almost everywhere and yet break spontaneously if triggered by a small highly stressed patch. Under the assumption of severe velocity-weakening friction (detailed in the previous section), a low level of prestress is required to achieve a reasonable stress drop.

To this end, we have considered here two effects rarely taken into account together in dynamic rupture scenarios: 1) increased fluid pressure and 2) deep stress concentrations. We discuss their trade offs in more detail in section A6. We infer that the interplay of deep creep, elevated fluid pressure and frictional dynamic weakening govern the apparent strength of faults and that these factors cannot be treated in isolation for such complex fault systems.

Further minor adjustments of the initial stresses are motivated by observations. To prevent excessive thrust faulting of the Kekerengu fault, we introduce a rotation of the maximum compressive stress orientation, within its range of uncertainty, from 100° in the South to 90° in the North. We also introduce a North-South increase of the seismogenic depth to allow deeper slip on the Papatea and Kekerengu faults, and a slight decrease of initial stress magnitude. Collectively both measures improve the model agreement with observed far-field ground deformations and rupture speed (they prevent shallow supershear rupture). Finally, we locally reduce the initial stresses on the Northernmost part of the Needles fault to prevent the occurrence of large slip in this area. We find that the Needles fault would otherwise host more than 10 m of slip, which is not supported by inversion results (Hamling et al., 2017; Xu et al., 2018).

1.4 Numerical method

We solve the coupled dynamic rupture and wave propagation problem using the freely available software SeisSol (Dumbser and Käser (2006), Pelties et al. (2014), https://github.com/SeisSol/SeisSol) based on the Arbitrary high-order accurate DERivative Discontinuous Galerkin method (ADER-DG). SeisSol employs fully adaptive, unstructured tetrahedral meshes to combine geometrically complex 3D geological structures, nonlinear rheologies and high-order accurate propagation of seismic waves. Our model (fig. 3) includes a geometrically complex fault network, high-resolution topography (Mitchell et al., 2012), 3D subsurface structure (Eberhart-Phillips et al., 2010) and plastic energy dissipation off the fault (Andrews, 2005, Wollherr et al., 2018). A high resolution model is crucial for accurately resolving rupture branching and (re-)nucleation processes. The degree of realism and accuracy achieved in this study is enabled by recent computational optimizations targeting strong scalability on many-core CPUs (Breuer et al., 2014, Heinecke et al., 2014, Rettenberger et al., 2016) and a ten-fold speedup owing to an efficient local time-stepping algorithm (Uphoff et al., 2017). Simulating 90 seconds on a computational mesh consisting of 29 million elements required typically 2 hours on 3000 Sandy Bridge cores of the supercomputer SuperMuc (Leibniz Supercomputing Centre, Germany), which is well within the scope of resources available to typical users of supercomputing centres. The few dynamic rupture simulations required to constrain the initial stress setup (methods sec. A7) employed a coarser discretization of wave propagation in the volume while still finely resolving the faults, reducing computational cost by 80%.

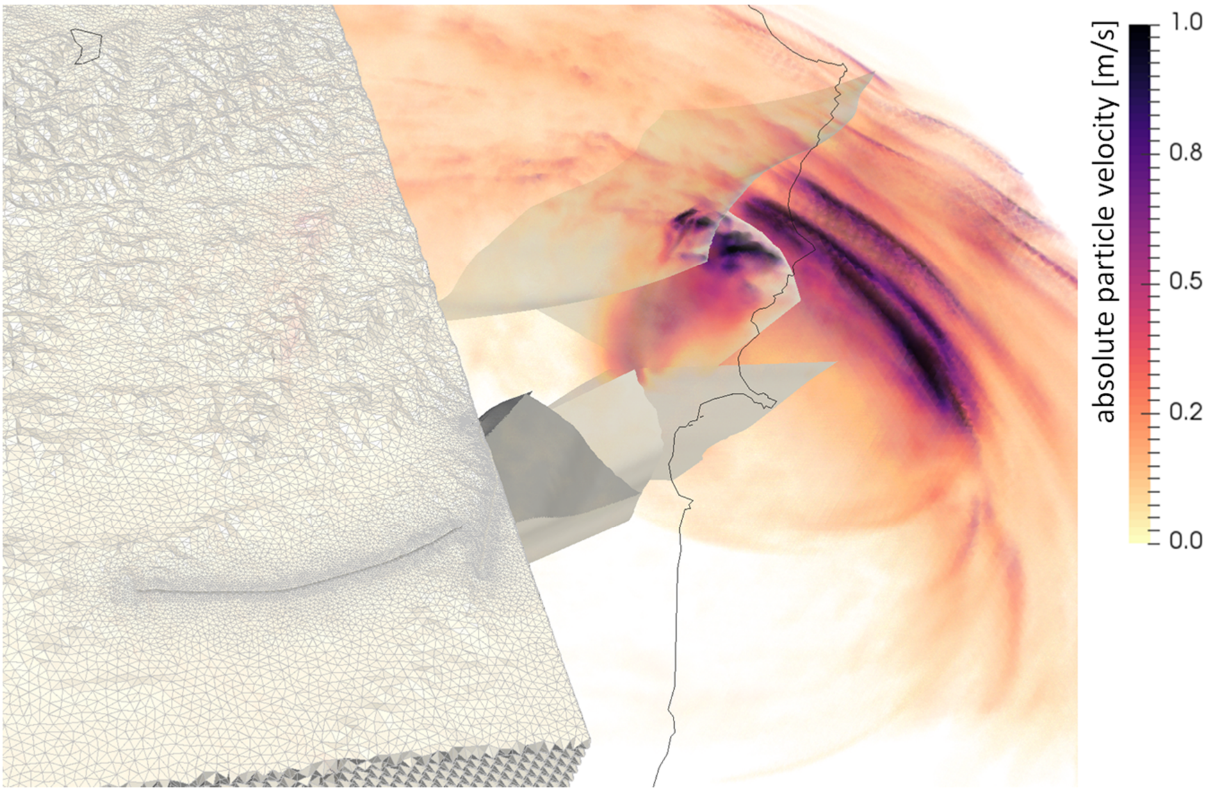

Figure 3: Snapshot of the wavefield (absolute particle velocity in m/s) across the fault network at a rupture time of 55 s. The model is discretized by an unstructured mesh accounting for 3D subsurface structure and high-resolution topography and featuring refined resolution in the vicinity of the faults. It incorporates the non-linear interactions between frictional on-fault failure, off-fault plasticity and wave propagation.

2. Results

In our dynamic model rupture propagates spontaneously across eight fault segments (fig. 1, which also shows three non-activated fault segments). The combined rupture length exceeds 240 km. The rupture successively cascades from South to North, directly branching at variable depths from the Humps to the Leader, Conwell-Charwell, Stone Jug, Hundalee and Point Kean faults. It then jumps to the Papatea fault via dynamic triggering at shallow depth, and finally branches to the Jordan Thrust, Kekerengu and Needles faults (fig. 4). This rupture cascade is dynamically viable without slip on the underlying subduction interface.

The modeled slip distributions and orientations are in agreement with the existing results (Xu et al., 2018, Clark et al., 2017). We observe an alternation of right-lateral strike-slip faulting (Humps, Conwell-Charwell, Jordan Thrust, Kekerengu and Needles faults) and thrusting (Leader, Hundalee and Papatea faults), as well as left-lateral strike-slip rupture of the Stone Jug fault and oblique faulting of the Point Kean fault (fig. 5). Due to the smoothness of our assumed initial stresses, the final slip distribution is less patchy than in source inversion models. However, the moment magnitude of 7.9 is in excellent agreement with observations (fig. 5f).

The complexity of the rupture cascade contributes to its apparently slow rupture speed. The ratio of rupture length to rupture duration (inferred from moment rate functions estimated by various authors; fig. 5f, Bai et al., 2017, Zhang et al., 2017, Vallée et al., 2011) indicates a slow average rupture velocity of about 1.4 km/s (Xu et al., 2018). In our model, rupture along each segment propagates twice as fast, at 2.9 km/s on average. Nevertheless, the observed rupture duration of approximately 90 s is reproduced thanks to a zigzagged propagation path accompanied by rupture delays at the transitions between segments (see animations in methods sec. A1). Specifically, the modeled rupture sequence takes about 30 s to reach the Hundalee fault after nucleation, whereas a hypothetical, uninterrupted rupture propagating at a constant speed of 3 km/s from the Humps to Hundalee faults would take only half this duration. The geometrical segmentation of the Leader and Conway-Charwell faults delays rupture by more than 5 s. Rupture across the Conway-Charwell fault is initiated at shallow depth. The Stone Jug fault can subsequently only be activated after rupture reached the deep stress concentration area and unleashed its triggering potential, causing further delay.

Specific episodes of the dynamic rupture model can be associated to prominent phases of moment release and high-frequency radiation observed in the Kaikōura earthquake. Abrupt changes in rupture velocity during the entangled Leader - Charwell-Conwell - Stone Jug fault transition 20 seconds after rupture onset may correspond to a burst of high-frequency energy (Madariaga, 1977) noted by back-projection studies (Zhang et al., 2017; Xu et al., 2018). Around 60 s after rupture onset, a distinct moment release burst lasting 20 s corresponds to the simultaneous failure of the Papatea and Kekerengu faults and is well aligned with observations (Bai et al., 2017, Zhang et al., 2017, Vallée et al., 2011).

The static ground deformation in our model is in good agreement with that inferred from geodetic data (Hamling et al., 2017, Xu et al., 2018, figs. 6 and 7). In particular, the maximum horizontal deformation along the Kekerengu fault and the substantial uplift near the intersection between the Papatea and Kekerengu faults are captured, and the observed ground deformation near the epicenter is reasonably replicated.

Strong ground motion and continuous GPS data provide valuable constraints on the rupture kinematics. We compare our simulation results to these data with a focus on the timing of pulses, because our model does not account for small scale heterogeneities which could significantly modulate waveforms. Due to the close distance of some of the stations to the faults (fig. 8) a close match of synthetic and observed waveforms is not expected. Yet, the dynamic rupture model is able to reproduce key features of the strong ground-motion and GPS recordings (fig. 9). Our model captures the shape and amplitude of some pronounced waveform pulses, e. g. of the first strong pulse recorded along the NS direction at GPS station MRBL, which is situated in the nucleation area. A time shift of around 2 s hints at a nucleation process slower than modeled. At near-fault station KEKS two dominant phases are visible on both observed and synthetics waveforms (at 52 s and 63 s after rupture onset in the NS synthetics of fig. 9 and in the fault-parallel-rotated waveforms of fig. S3). These dominant phases were attributed to a slip reactivation process on the Kekerengu fault by Holden et al. (2017). However, our model suggests that the first peak stems from the earlier rupture of the Papatea segment (see animation A1.B). The ground motions recorded at station KEKS are thus consistent with a sequential rupture from the Papatea to Kekerengu faults. Strong evidence for a rupture sequence from Papatea to Kekerengu is further provided by the teleseismic back-projection results of Xu et al (2018). More recently, comparing remote sensing and field observations to 2D dynamic simulation results, Klinger et al. (2018) showed that observed patterns of surface slip and off-fault damage support this scenario.

Our model without slip on the subduction interface satisfactorily reproduces long-period teleseismic data. Synthetics are generated at 5 teleseismic stations around the event (fig. 8). We translate the dynamic fault slip time histories of our model into a subset of 40 double couple point sources. From these sources, broadband seismograms are calculated from a Green’s function database using Instaseis (Krischer et al., 2017) and the PREM model for a maximum period of 10 s including anisotropic effects. In the long period range considered

(100 to 450 s) the fit to observations is satisfying (fig. 10). The effect of gravity, significant for surface waves at those periods, is not accounted for in the synthetics due to methodological limitations of Instaseis. In conjunction with our restriction to the 1D PREM model instead of incorporating 3D subsurface information, remaining differences between synthetics and observed records are expected. Following the same approach but based on Duputel and Riviera (2017)'s kinematic source model inferred from teleseismic data, indeed yields similar discrepancies. Overall, our results imply that slip on the subduction interface is not required to explain teleseismic observables.

There is a high level of uniqueness in the outcome of our dynamic model. Slight variations on the initial conditions, for instance a subtle change in the maximum principal stress direction of 10 degrees or a less transpressional regime (e.g. a 10% increase of the stress shape ratio defined in eq. 9 of methods secs. A6), lead to early spontaneous rupture arrest. Changes in fault geometry (orientation, size and separation distance of fault segments) also affect the dynamics considerably. Moreover, ad hoc abrupt lateral changes in initial fault stress or strength are not required to steer the rupture along its zigzagged path. We nevertheless acknowledge the possibility of alternative models yielding similar rupture dynamics. Such models can be readily designed based on the trade-offs we define in methods sec. A6, e. g. by decreasing or increasing the effects of deep stress concentrations, fluid pressure or frictional weakening. In methods sec. A7, we accordingly ensure the robustness of important modelling choices of the preferred model.

Two segments, the Stone Jug and the Point Kean faults, are crucial for the successful propagation of the rupture to the North. The Stone Jug fault hosts little slip but allows the earthquake to branch towards the Hundalee fault. The offshore Point Kean fault links at depth the seemingly disconnected Southern and Northern parts of the fault system (as proposed by Cesca et al., 2017), whose surface traces are separated by a large gap of 15 km. Our model matches the observed (horizontal) surface rupture in the Northern part

(Litchfield et al., 2017), the inferred slip amplitude and the northwards rupture propagation on the Point Kean fault, by dominantly oblique faulting. It supports a previous suggestion that rupture of the Point Kean fault was responsible for the observed on-shore coastal uplift extending 20 km north of Kaikōura Peninsula (Clark et al., 2017). On the other hand, a stronger dip-slip component would be required to explain the northeastward GPS displacements around this thrust fault. According to the dynamic rupture model, this could only be achieved by an (unlikely) local prestress rotation of about 30 degrees towards South, or by considering a fault geometry with lower strike.

The dynamic model shows rupture complexity also at a fine scale. Rupture takes the form of slip-pulses (fig. 4) of various origins: fast-velocity weakening friction promotes self-healing slip pulses (Heaton, 1990, Gabriel et al., 2012) which can propagate at lower background stress levels and with smaller slip than crack-like ruptures. The nonlinear interaction between frictional failure and the free surface causes interface waves that bounce back from the surface, fault ends and branching points lead to rupture front segmentation, unloading stresses carried by seismic waves reflected from subsurface impedance contrasts cause healing fronts. The Hundalee, Point Kean, Papatea and Kekerengu segments slip more than once.

Rupture complexity can affect seismological inferences of fault friction properties. Frictional parameters are typically adopted from laboratory experiments. However, it is uncertain how valid it is to extrapolate results from the laboratory scale to the field scale. For the Kaikōura earthquake, a large slip-weakening distance D_c, the amount of slip over which frictional weakening occurs, has been estimated from a strong-motion record (Kaneko et al., 2017). Despite the much smaller on-fault D_c values (0.2 to 0.5 m) in our model, the apparent D_c value inferred from the resulting off-fault ground motions is large (5.6 m, fig. S4), which can be attributed to intertwined waveforms from multiple slip fronts.

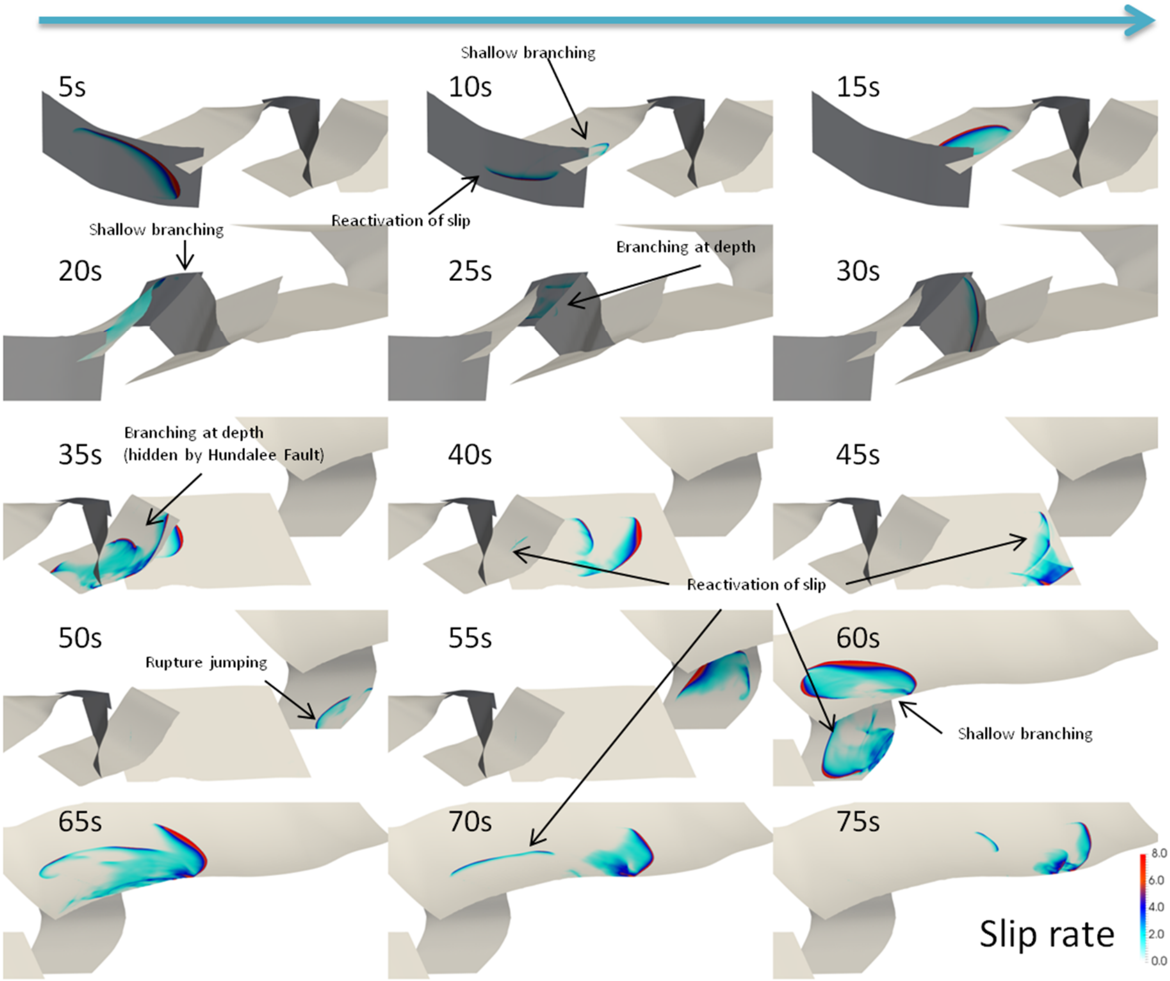

Figure 4: Overview of the simulated rupture propagation. Snapshots of the absolute slip rate are shown every 5 s. The figure focuses on four different portions of the fault system, following the rupture front as it propagates from South to North. Labels indicate remarkable features of the rupture discussed in the text.

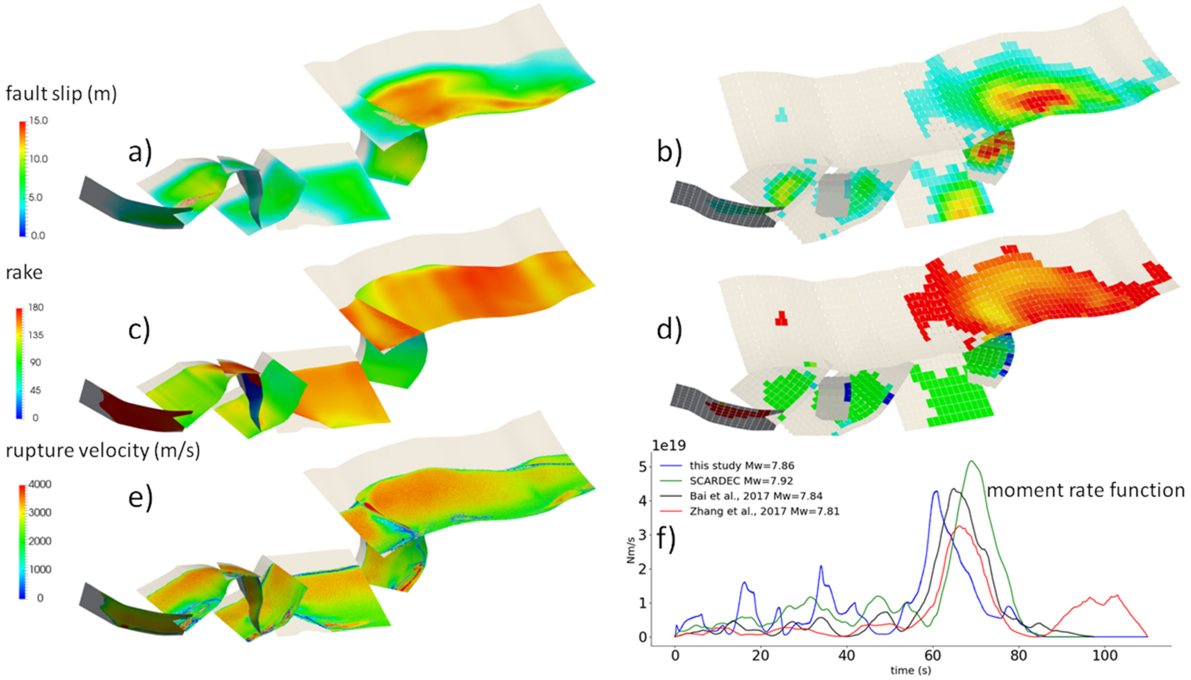

Figure 5: Source properties of the dynamic rupture model and comparison to observational inferences. Final slip magnitude (a) modeled here and (b) inferred by Xu et al. (2018). Final rake angle (c) modeled and (d) inferred by Xu et al. (2018). (e) Modeled rupture velocity. (f) Modeled moment rate function compared with those inferred by Bai et al. (2017) from teleseismic and tsunami data, by Zhang et al. (2017) from seismic waveform inversion and from teleseismic data by the SCARDEC method (Vallée et al., 2011).

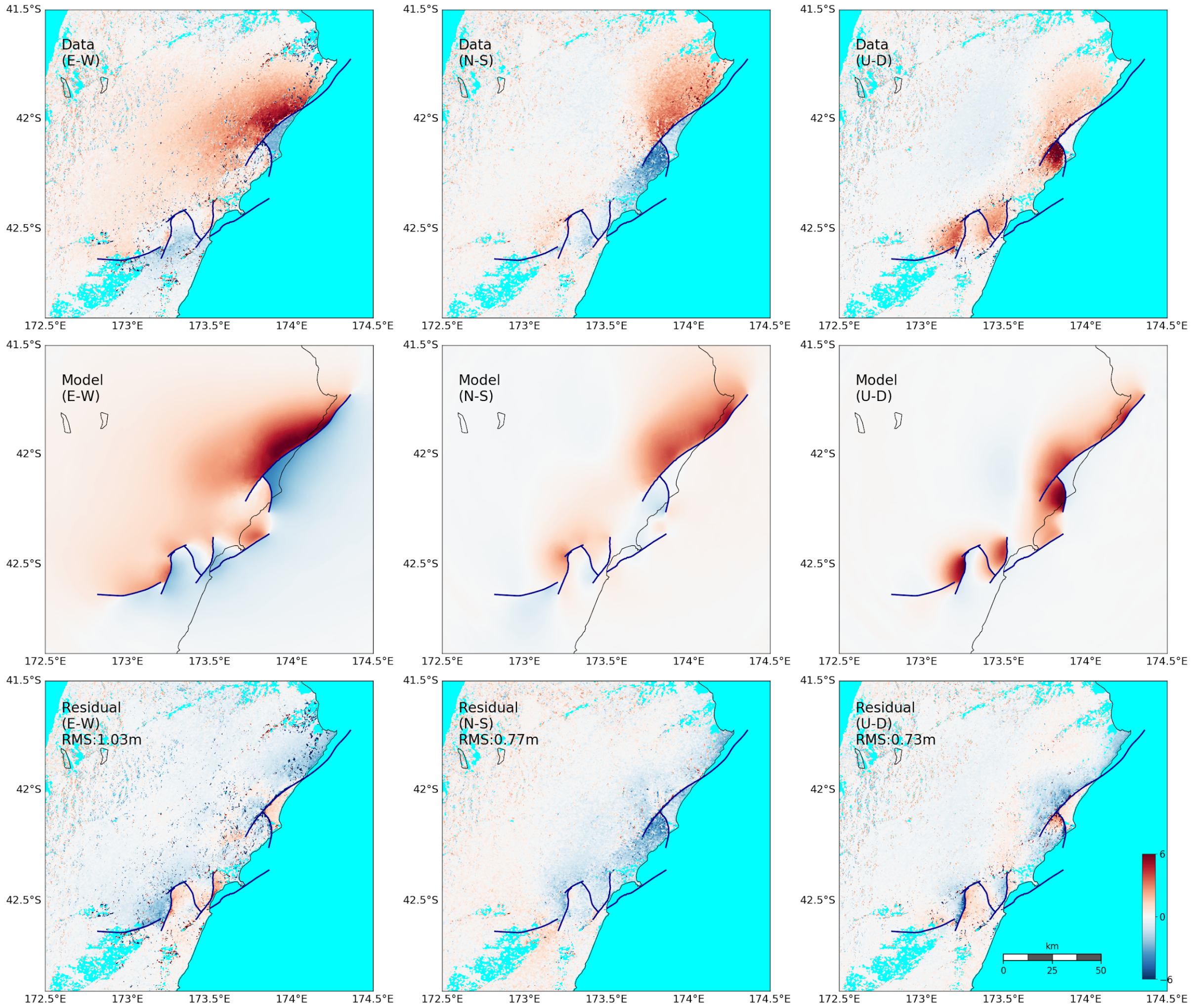

Figure 6: Comparison of observed and modeled coseismic surface displacements. 3D ground displacement (first row) inferred by space geodetic data (Xu et al. 2018), (second row) generated by the dynamic rupture model and (third row) their difference, all in meters. Columns from left to right are EW, NS and UD components. Root-mean-square (RMS) misfits are provided in the third row for each component.

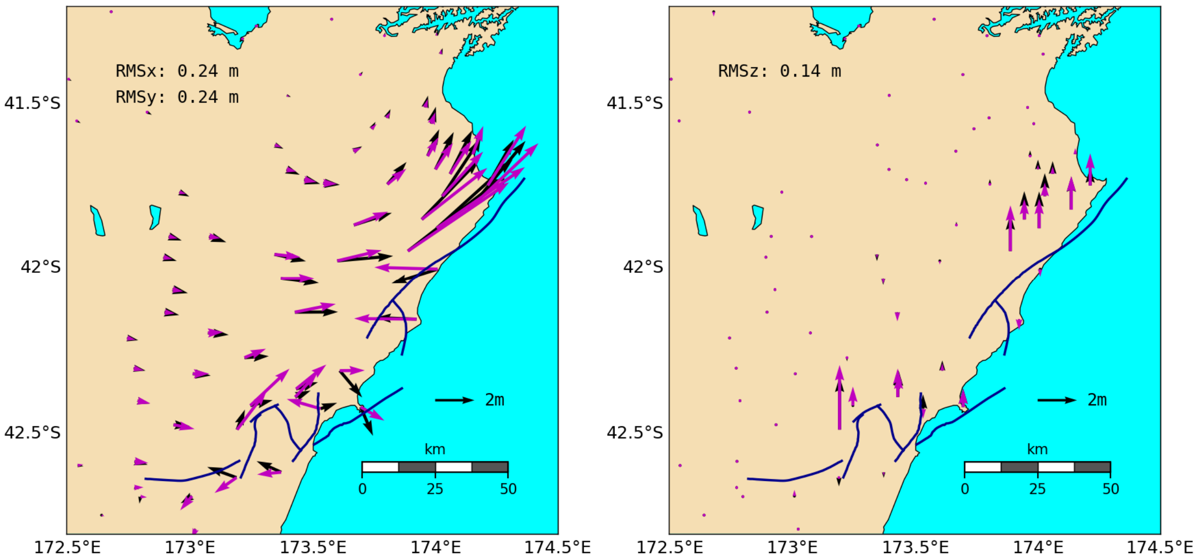

Figure 7: Comparison of observed (black, Hamling et al. 2017) and modeled (magenta) horizontal (left) and vertical (right) ground displacement at GPS stations. Root-mean-square (RMS) misfits are provided for each component.

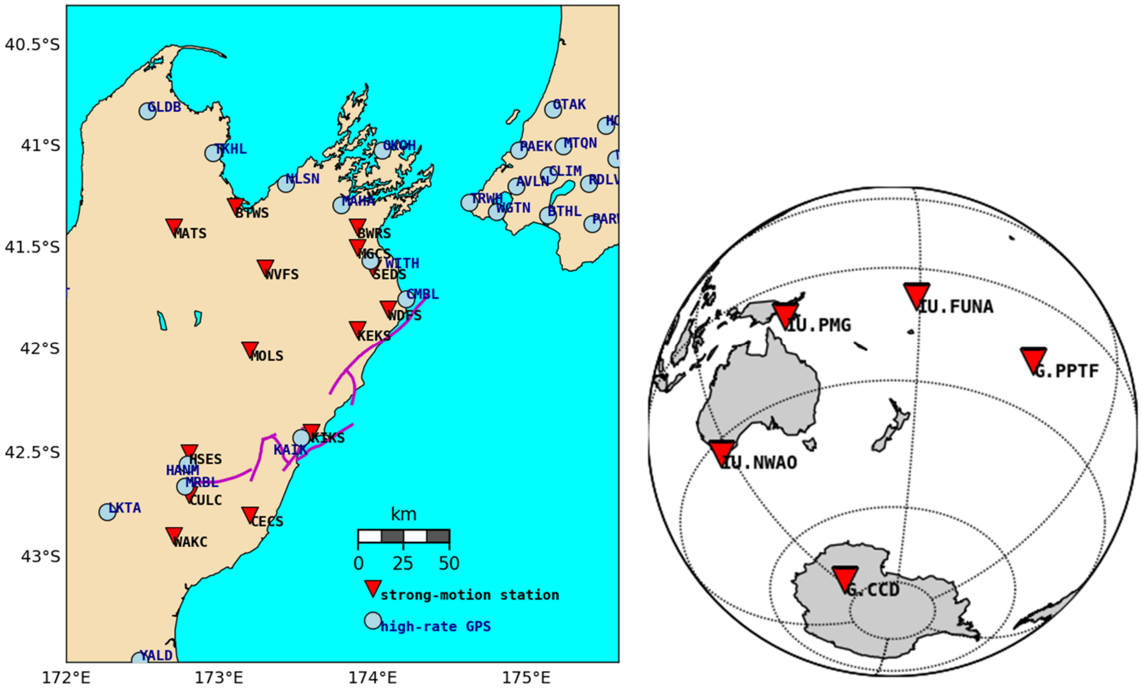

Figure 8: Nearest high-rate GPS and strong-motion stations (on South Island) active during the Kaikoura earthquake (left). Teleseismic stations at which synthetic data is compared with observed records (right).

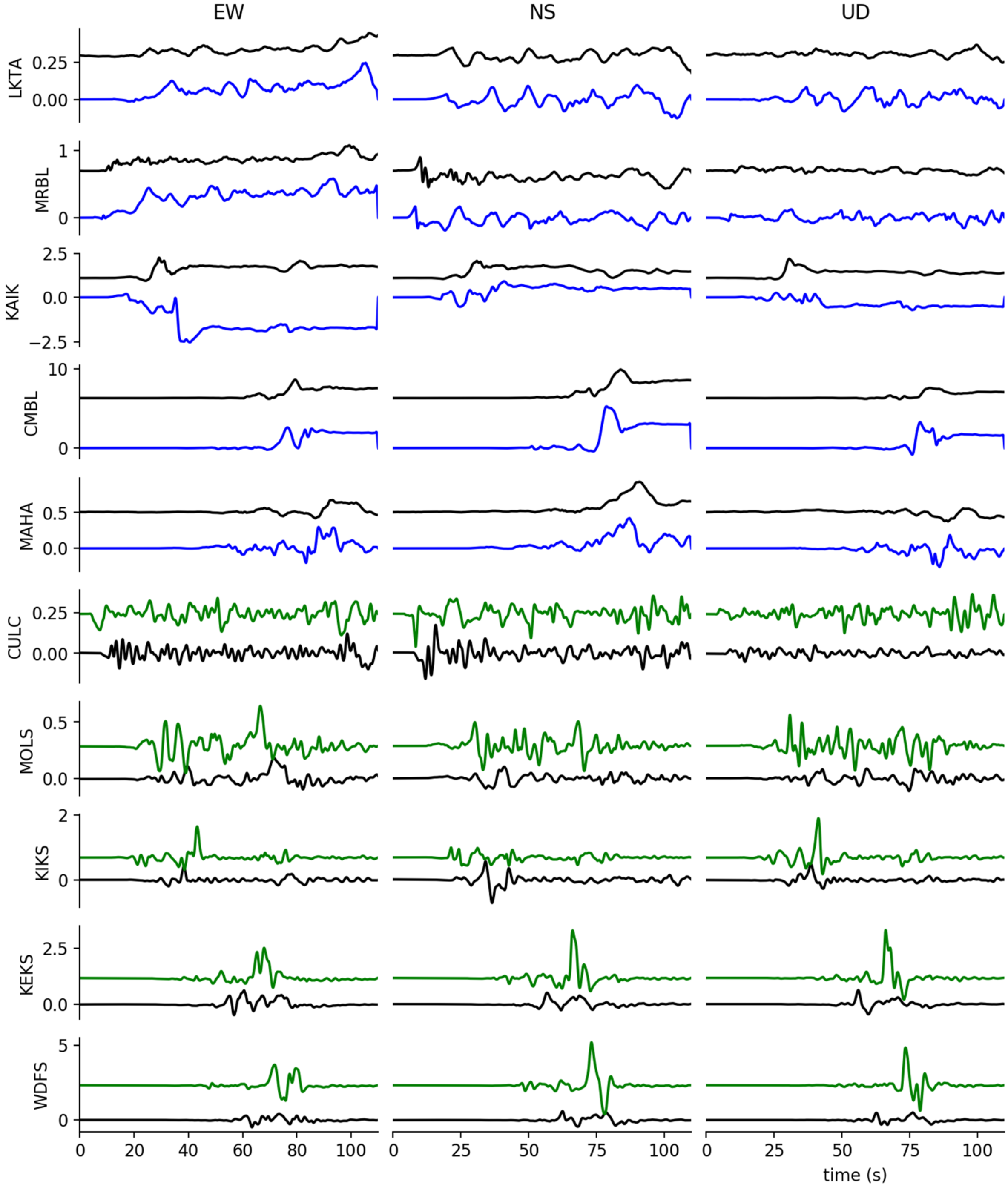

Figure 9: Comparison of modelled and observed ground motions. Five top rows: synthetic (blue) and observed (black) ground displacements at selected GPS stations. A 1 s low-pass filter has been applied to both signals. Five bottom rows: synthetic (green) and observed (black) ground velocities at selected strong-motion stations. A 0.005-1 s band-pass filter has been applied to both signals. The station locations are shown in Figure 8.

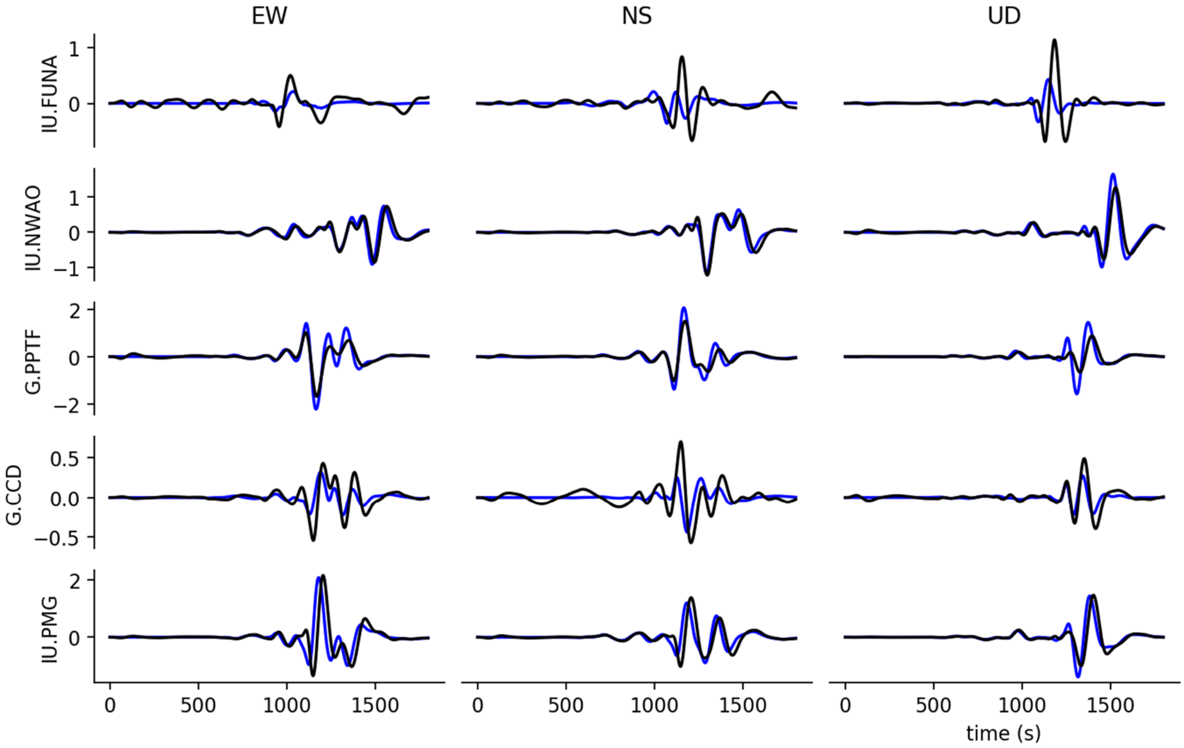

Figure 10: Comparison of modeled (blue) and observed (black) teleseismic waveforms. A 100-450 s band-pass filter is applied to all traces. Synthetics are generated using Instaseis (Krischer et al., 2017) and the PREM model including anisotropic effects and a maximum period of 10 s.

3. Discussion

The physics-based dynamic source modeling approach in this study has distinct contributions compared to the data-driven kinematic source modeling approach. In the latter, a large number of free parameters enables close fitting of observations at the expense of mechanical consistency. Furthermore, the kinematic earthquake source inversion problem is inherently non-unique (many solutions fit the data equally well). In contrast, our dynamic model is controlled by a few independent parameters. Its main goal is to understand the underlying physics of the cascading rupture sequence. Adopting fault geometries and a regional stress state consistent with previous studies, our dynamic rupture model reproduces major observations of the real event, reveals unexpected features and constrains competing hypotheses.

Our results provide insight on the state of stress under which complex fault systems operate. In our model, strong frictional weakening, fluid overpressure and deep stress concentrations result in a remarkably low apparent friction. Yet the low average ratio of initial shear stress to normal stress does not hinder dynamic rupture cascading across multiple fault segments. Instead, it is crucial to achieve the full cascading rupture with realistic stress drop and slip. In methods sec. A7 we discuss fault strength based on the orientation of the fault system, apparent fault strengths in the static and dynamic sense and explore additional model setups demonstrating the robustness of our preferred model. We conclude by quantifying the relative contributions of our modeling assumptions to the apparent weakness of faults.

The effects of overpressurized fault fluids and deep stress concentrations and the additional effect of a low dynamic friction result in an overall low apparent friction coefficient. We find that reproducing all aspects of the rupture cascade requires all three effects. The combined effect of strong frictional weakening, fluid overpressure and deep stress concentrations and the fundamental impact of fault weakness on the existence of subduction and tectonics (e.g. Osei Tutu et al., 2018) show the importance of mechanical feedbacks across multiple time scales, from the short-term processes of dynamic rupture and earthquake cycles to the long-term geodynamic processes that shape and reshape the Earth.

Dramatic frictional weakening is one of the key mechanisms contributing to fault weakness in our model. Our assumed dynamic friction coefficient, f_w=0.1, falls within the range of values typically observed in laboratory experiments and considered by the dynamic rupture community (e.g. Noda et al., 2009; Gabriel et al., 2012; Shi and Day, 2013). Nevertheless, we probed the necessity of such a low value by additional simulations, as detailed in methods sec. A7d. By static considerations, we find that a sustained cascading rupture under a higher f_w would require conditions that disagree with stress inversion inferences, namely a too low stress shape ratio (Fig. S5). In addition, prescribing higher f_w results in a prestress distribution of larger variability, less favourable for rupture cascading.

Frictional failure in our model initiates at the best-oriented fault segment, in contrast with the 'keystone fault' model (Fletcher et al., 2016) in which large multi-fault earthquakes nucleate on a misoriented fault. The dynamic rupture cascade does not require laterally heterogeneous initial stresses, as those arising on fault networks in which optimally oriented faults release stress not only during large earthquakes but also via smaller events or aseismic creep.

We find that a zigzagged propagation path, accompanied by rupture delays at the transitions between faults, can explain apparently slow rupture speeds. While the surprisingly slow apparent rupture velocity and long rupture duration were depicted widely in seismological observations, our dynamic model provides a mechanically viable explanation for this observation.

Physics-based dynamic modeling contributes crucial arguments to the debate of whether the rupture of multiple crustal faults during the Kaikōura earthquake was promoted by slip on the underlying Hikurangi subduction interface. Rupture of the subduction interface is not favored by the regional stresses we inferred. A planar, shallowly dipping subduction interface approximated similar to previous studies (Hamling et al., 2017) experiences very low shear stresses when included in our model. Dynamic triggering of such a subduction interface is further impeded by its large depth below the crustal fault network. However, slip may be promoted if the stresses rotate at depth or if the megathrust is frictionally weaker than the crustal faults (e.g. Suppe, 2014., Hardebeck et al., 2015). We show that incorporating the shallowly dipping (35°) Point Kean fault segment successfully links the Southern and Northern parts of the fault system without involvement of the Hikurangi subduction interface. Our model is equally compatible with long-period teleseismic data as models assuming slip on the subduction interface and may be further tested by tsunami observations.

Features of the Kaikōura earthquake that remain unexplained by our dynamic models suggest opportunities to better understand the role of fault heterogeneities. These features include the inferred localized slip at depth on the Upper Kowhai fault as well as incompletely modeled aspects of the observed waveforms. Our dynamic rupture scenario is able to explain the early rupture termination to the South, but does not give a definitive answer concerning the origin of rupture termination to the North. On the Humps fault zone, spontaneous rupture termination to the West is observed, associated with a slight change in the strike direction resulting in a less favorable fault orientation. In additional dynamic rupture simulations including the nearest identified faults to the South, the Leonard Mound and the Culverden reverse faults (e.g. Pettinga et al., 2001), we found that the rupture is not able to trigger those faults. To the North, we have to locally reduce the initial stresses on the Northernmost part of the Needles fault to prevent its rupture with large slip. The very straight surface rupture of the Needles fault (Litchfield et al., 2017) does not suggest a high segmentation that may have prevented the rupture to extend further North. Hamling et al. (2017) and Wang et al. (2017) suggest a steeper geometry for this segment (dip angle of 70°) which would result in an increased shear over normal stress ratio, favouring rupture instead of terminating it. These considerations indicate that the most likely reason for the rupture termination to the North is the presence of an asperity to which the many aftershocks in the region (Kaiser el al., 2017) might be associated.

Our model provides a solution to one of the fundamental riddles of the Kaikoura earthquake: why did the rupture by-pass the Hope fault? The lack of significant slip observed on the

Hope fault is surprising given its orientation similar to the Kekerengu fault, its fast geologic slip-rate and short recurrence interval (180-310 years, Stirling et al. (2017) and references therein), and its linkage to most mapped faults involved in the rupture. In our model, the Hope and Conway-Charwell faults are less than 1 km apart at the surface, and diverge at depth because of their different dipping angles. Both faults are well oriented relative to the background stress. Yet, the Hope fault is not triggered by the rupture of the Conway-Charwell fault, nor later on by the rupture of the Hundalee and Point Kean faults. We interpret this non-rupture as a consequence of the restraining step-over configuration formed by the Conway-Charwell and Hope faults, leading to an unfavourable distribution of dynamic stresses on the Hope fault (e.g. Oglesby, 2005). Dynamic modeling allows assessing the possibility of rupture jumping across such unconventional stepover configurations, combining thrust and strike-slip faulting mechanisms and faults of different dip angles.

Dynamic rupture modeling is now approaching a state of maturity and computational efficiency that should soon allow it to be integrated synergistically with data inversion efforts within the first days following the occurrence of an earthquake, making physics-based interpretations an important part of the rapid earthquake response toolset.

Acknowledgments

The work presented in this paper was supported by the German Research Foundation (DFG) (projects no. KA 2281/4-1, GA 2465/2-1, GA 2465/3-1), by BaCaTec (project no. A4), by KONWIHR - the Bavarian Competence Network for Technical and Scientific High Performance Computing (project NewWave), by the Volkswagen Foundation (grant no. 88479), by KAUST-CRG (grant no. ORS-2016-CRG5-3027), by the European Union's Horizon 2020 research and innovation program (grant no. 671698), by NSF CAREER award EAR-1151926, by the French government through the UCAJEDI Investments in the Future project ANR-15-IDEX-01 managed by the National Research Agency (ANR), by the Hong

Kong Polytechnic University startup grant (1-ZE6R) and by the Hong Kong Research Grants Council Early Career Scheme Fund (F-PP4B). Computing resources were provided by the Leibniz Supercomputing Centre (LRZ, projects no. h019z, pr63qo, and pr45fi on SuperMUC). We thank J. Townend for sharing his stress inversion data, J. Zhang and M. Vallée for sharing moment rate functions, C. Holden and E. d'Anastasio who provided processed GPS time-series, GNS Science for providing active fault database, earthquake rupture maps and reports, continuous GPS data, and strong motion waveform data and the editor and two anonymous reviewers for their positive feedback and thoughtful reviews.

Author contributions

This project was initiated by J.-P. A. Modelling was conducted by T. U. under the supervision of A.-A. G. with input from J.-P. A. and W. X. The manuscript was written jointly by T. U., A.-A. G. and J.-P. A.

Competing interests

The authors declare no competing financial interests.

References

1. Hamling, I. J. et al. (2017). Complex multifault rupture during the 2016 Mw 7.8 Kaikōura earthquake, New Zealand. *Science*, **356** (6334), 7194.

2. Duputel, Z., and Rivera, L. (2017). Long-period analysis of the 2016 Kaikoura earthquake. *Physics of the Earth and Planetary Interiors*, **265**, 62-66.

3. Bradley, B. A., Razafindrakoto, H. N., and Polak, V. (2017). Ground□Motion Observations from the 14 November 2016 M w 7.8 Kaikoura, New Zealand, Earthquake and Insights from Broadband Simulations. *Seismological Research Letters*, **88** (3), 740-756.

4. Holden, C. et al. (2017). The 2016 Kaikōura Earthquake Revealed by Kinematic Source Inversion and Seismic Wavefield Simulations: Slow Rupture Propagation on a Geometrically Complex Crustal Fault Network. *Geophysical Research Letters*, **44** (22), 11320-11328.

5. Wang, T. et al. (2018). The 2016 Kaikōura earthquake: Simultaneous rupture of the subduction interface and overlying faults. *Earth and Planetary Science Letters*, **482**, 44-51.

6. Hollingsworth, J., Ye, L., and Avouac, J. P. (2017). Dynamically triggered slip on a splay fault in the Mw 7.8, 2016 Kaikoura (New Zealand) earthquake. *Geophysical Research Letters*, **44** (8), 3517-3525.

7. Xu, W. et al. (2018). Transpressional Rupture Cascade of the 2016 M_w 7.8 Kaikoura Earthquake, New Zealand. *Journal of Geophysical Research: Solid Earth*, **123**.

8. Zhang, H., Koper, K. D., Pankow, K., and Ge, Z. (2017). Imaging the 2016 MW 7.8 Kaikoura, New Zealand Earthquake with Teleseismic P Waves: A Cascading Rupture Across Multiple Faults. *Geophysical Research Letters*, **44**, 4790-4798.

9. Bai, Y., Lay, T., Cheung, K. F., and Ye, L. (2017). Two regions of seafloor deformation generated the tsunami for the 13 November 2016, Kaikoura, New Zealand earthquake. *Geophysical Research Letters*, **44** (13), 6597-6606.

10. Clark, K. J. et al. (2017). Highly variable coastal deformation in the 2016 Mw7. 8 Kaikōura earthquake reflects rupture complexity along a transpressional plate boundary. *Earth and Planetary Science Letters*, **474**, 334-344.

11. Cesca, S. et al. (2017). Complex rupture process of the Mw 7.8, 2016, Kaikoura earthquake, New Zealand, and its aftershock sequence. *Earth and Planetary Science Letters*, **478**, 110-120.

12. Williams, C. A. et al. (2013). Revised interface geometry for the Hikurangi subduction zone, New Zealand. *Seismological Research Letters*, **84**(6), 1066-1073.

13. Bai, K., and Ampuero, J. P. (2017). Effect of Seismogenic Depth and Background Stress on Physical Limits of Earthquake Rupture Across Fault Step Overs. *Journal of Geophysical Research: Solid Earth*, **122** (12), 10280-10298.

14. Gabriel, A.-A., Ampuero, J. P., Dalguer, L. A., and Mai, P. M. (2012). The transition of dynamic rupture styles in elastic media under velocity‐weakening friction. *Journal of Geophysical Research: Solid Earth*, **117** (B9), B09311.

15. Shi, Z., and Day, S. M. (2013). Rupture dynamics and ground motion from 3-D rough‐fault simulations. *Journal of Geophysical Research: Solid Earth*, **118** (3), 1122-1141.

16. Aochi, H., and Ulrich, T. (2015). A probable earthquake scenario near Istanbul determined from dynamic simulations. *Bulletin of the Seismological Society of America*, ***105*** (3), 1468-1475.

17. Olsen, K. B., Madariaga, R., and Archuleta, R. J. (1997). Three-dimensional dynamic simulation of the 1992 Landers earthquake. *Science*, **278** (5339), 834-838.

18. Ma, Custódio, Archuleta, and Liu (2008), Dynamic modeling of the 2004 Mw 6.0 Parkfield, California, earthquake, *J. Geophys. Res.*, **113**, B02301.

19. Zoback, et al. (1987). New evidence on the state of stress of the San Andreas fault system. *Science*, **238**(4830), 1105-1111.

20. Behr, W. M., & Platt, J. P. (2014). Brittle faults are weak, yet the ductile middle crust is strong: Implications for lithospheric mechanics. *Geophysical Research Letters*, **41**(22), 8067-8075.

21. England, P. (2018). On shear stresses, temperatures, and the maximum magnitudes of earthquakes at convergent plate boundaries. *Journal of Geophysical Research: Solid Earth*, **123**(8), 7165-7202.

22. Duarte, J. C., Schellart, W. P., & Cruden, A. R. (2015). How weak is the subduction zone interface?. *Geophysical Research Letters*, **42**(8), 2664-2673.

23. Osei Tutu, A., Sobolev, S. V., Steinberger, B., Popov, A. A., and Rogozhina, I. (2018). Evaluating the influence of plate boundary friction and mantle viscosity on plate velocities. *Geochemistry, Geophysics, Geosystems*, **19.**

24. Byerlee, J. D. (1978) Friction of Rocks. *Pure and Applied Geophysics*. **116** (4-5), 615–626.

25. Noda, H., Dunham, E. M., & Rice, J. R. (2009). Earthquake ruptures with thermal weakening and the operation of major faults at low overall stress levels. *Journal of Geophysical Research: Solid Earth*, **114**(B7).

26. Litchfield, N. J., et al. (2014). A model of active faulting in New Zealand. *New Zealand Journal of Geology and Geophysics*, **57**(1), 32-56.

27. Nicol, A., et al. (2018). Preliminary geometry, displacement, and kinematics of fault ruptures in the epicentral region of the 2016 M w 7.8 Kaikōura, New Zealand, earthquake. *Bulletin of the Seismological Society of America*, https://doi.org/10.1785/0120170329

28. Dunham, E. M., Belanger, D., Cong, L., and Kozdon, J. E. (2011). Earthquake ruptures with strongly rate-weakening friction and off-fault plasticity, Part 1: Planar faults. *Bulletin of the Seismological Society of America*, **101**(5), 2296-2307.

29. Di Toro, G. et al. (2011). Fault lubrication during earthquakes. *Nature*, **471** (7339), 494.

30. Andrews, D. J. (1976). Rupture propagation with finite stress in antiplane strain. *Journal of Geophysical Research*, ***81*** (20), 3575-3582.

31. Copley, A. (2018). The strength of earthquake-generating faults. *Journal of the Geological Society*, **175** (1), 1-12.

32. Hardebeck, J. L. (2015). Stress orientations in subduction zones and the strength of subduction megathrust faults. *Science*, **349** (6253), 1213-1216.

33. Townend, J., Sherburn, S., Arnold, R., Boese, C., and Woods, L. (2012). Three-dimensional variations in present-day tectonic stress along the Australia–Pacific plate boundary in New Zealand. *Earth and Planetary Science Letters*, **353**, 47-59.

34. Aochi, H., and Madariaga, R. (2003). The 1999 Izmit, Turkey, earthquake: Nonplanar fault structure, dynamic rupture process, and strong ground motion. *Bulletin of the Seismological Society of America*, **93** (3), 1249-1266.

35. Suppe, J. (2014). Fluid overpressures and strength of the sedimentary upper crust. *Journal of Structural Geology*, **69**, 481-492.

36. Sutherland, R. et al. (2017). Extreme hydrothermal conditions at an active plate-bounding fault. *Nature*, **546** (7656), 137.

37. Uphoff, C., Rettenberger, S., Bader, M., Madden, E. H., Ulrich, T., Wollherr, S., and Gabriel, A.-A. (2017). Extreme scale multi-physics simulations of the tsunamigenic 2004 Sumatra megathrust earthquake. In *Proceedings of the International Conference for High Performance Computing, Networking, Storage and Analysis,* SC’17, 21, 1-16.

38. Aochi, H., Cushing, M., Scotti, O., and Berge-Thierry, C. (2006). Estimating rupture scenario likelihood based on dynamic rupture simulations: The example of the segmented Middle Durance fault, southeastern France. *Geophysical Journal International*, **165** (2), 436-446.

39. Kato, N. (2012). Fracture energies at the rupture nucleation points of large interplate earthquakes. *Earth and Planetary Science Letters*, **353**, 190-197.

40. Bruhat, L., and Segall, P. (2017). Deformation rates in northern Cascadia consistent with slow updip propagation of deep interseismic creep. *Geophysical Journal International*, **211**(1), 427-449.

41. Ader, T., et al. (2012). Convergence rate across the Nepal Himalaya and interseismic coupling on the Main Himalayan Thrust: Implications for seismic hazard. *Journal of Geophysical Research: Solid Earth*, **117** (B4), B04403.

42. Mildon, Z. K., Roberts, G. P., Faure Walker, J. P., & Iezzi, F. (2017). Coulomb stress transfer and fault interaction over millennia on non-planar active normal faults: the Mw 6.5–5.0 seismic sequence of 2016–2017, central Italy. *Geophysical Journal International*, ***210***(2), 1206-1218.

43. Lamb, S., Arnold, R., & Moore, J. D. (2018). Locking on a megathrust as a cause of distributed faulting and fault-jumping earthquakes. *Nature Geoscience*, 1, https://doi.org/10.1038/s41561-018-0230-5

44. Dumbser, M. and Käser, M. (2006). An Arbitrary High Order Discontinuous Galerkin Method for Elastic Waves on Unstructured Meshes II: The Three-Dimensional Isotropic Case. *Geophysical Journal International*, **167**(1), 319-336.

45. Pelties, C., Gabriel, A.-A., and Ampuero, J. P. (2014). Verification of an ADER-DG method for complex dynamic rupture problems. *Geoscientific Model Development*, **7** (3), 847-866.

46. Mitchell, J. S. et al. (2012). Undersea New Zealand, 1:5,000,000.

47. Eberhart-Phillips, D., Reyners, M., Bannister, S., Chadwick, M., and Ellis, S. (2010). Establishing a versatile 3-D seismic velocity model for New Zealand. *Seismological Research Letters*, **81** (6), 992-1000.

48. Andrews, D. J. (2005). Rupture dynamics with energy loss outside the slip zone. *Journal of Geophysical Research: Solid Earth*, **110** (B1), B01307.

49. Wollherr, S., Gabriel, A. A., & Uphoff, C. (2018). Off-fault plasticity in three-dimensional dynamic rupture simulations using a modal Discontinuous Galerkin method on unstructured meshes: Implementation, verification, and application. *Geophysical Journal International*, ggy213, https://doi.org/10.1093/gji/ggy213.

50. Breuer, A. et al. (2014). Sustained petascale performance of seismic simulations with SeisSol on SuperMUC. In *International Supercomputing Conference,* ISC 2014, 8488, 1-18.

51. Heinecke, A. et al. (2014). Petascale high-order dynamic rupture earthquake simulations on heterogeneous supercomputers. In *Proceedings of the International Conference for High Performance Computing, Networking, Storage and Analysis*, SC'14, 3-14.

52. Rettenberger, S., Meister O., Bader M., and Gabriel A.-A. (2016), ASAGI - A Parallel Server for Adaptive Geoinformation. In *2016 Exascale Applications and Software Conference Proceedings,* EASC'16, 2, 1-9.

53. Vallée, M., Charléty, J., Ferreira, A. M., Delouis, B., and Vergoz, J. (2011). SCARDEC: a new technique for the rapid determination of seismic moment

magnitude, focal mechanism and source time functions for large earthquakes using body-wave deconvolution. *Geophysical Journal International*, **184** (1), 338-358.

54. Madariaga, R. (1977). High-frequency radiation from crack (stress drop) models of earthquake faulting. *Geophysical Journal International*, **51** (3), 625-651.

55. Klinger, Y. et al. (2018). Earthquake damage patterns resolve complex rupture processes. *Geophysical Research Letters*, https://doi.org/10.1029/2018GL078842

56. Krischer, L., Hutko, A. R., Driel, M. van, Stähler, S., Trabant, C., and Nissen-Meyer, T. (2017). On-demand custom broadband synthetic seismograms. *Seismological Research Letters*, **88**(4).

57. Litchfield N. J., et al. (2017). 14th November 2016 M7.8 Kaikoura Earthquake. Summary surface fault rupture traces and displacement measurements. GNS Science.

58. Heaton, T. H. (1990). Evidence for and implications of self-healing pulses of slip in earthquake rupture. *Physics of the Earth and Planetary Interiors*, **64** (1), 1-20.

59. Kaneko, Y., Fukuyama, E., and Hamling, I. J. (2017). Slip-weakening distance and energy budget inferred from near□fault ground deformation during the 2016 Mw7. 8 Kaikōura earthquake. *Geophysical Research Letters,* **44** (10), 4765-4773.

60. Fletcher, J. M., Oskin, M. E., and Teran, O. J. (2016). The role of a keystone fault in triggering the complex El Mayor-Cucapah earthquake rupture. *Nature Geoscience*, **9** (4), 303-307.

61. Pettinga, J. R., Yetton, M. D., Van Dissen, R. J., & Downes, G. (2001). Earthquake source identification and characterisation for the Canterbury region, South Island, New Zealand.

62. Kaiser, A. et al. (2017). The 2016 Kaikōura, New Zealand, earthquake: preliminary seismological report. *Seismological Research Letters*, **88**(3), 727-739.

63. Stirling, M. W. et al. (2017). The Mw 7.8 2016 Kaikōura earthquake: Surface fault rupture and seismic hazard context. *Bull. New Zeal. Soc. Earthq. Eng.*, **50** (2), 73-84.

64. Oglesby, D. D. (2005). The dynamics of strike-slip step-overs with linking dip-slip faults. *Bulletin of the Seismological Society of America*, **95**(5), 1604-1622.

65. Mikumo, T., Olsen, K. B., Fukuyama, E., and Yagi, Y. (2003). Stress-breakdown time and slip-weakening distance inferred from slip-velocity functions on earthquake faults. *Bulletin of the Seismological Society of America*, **93** (1), 264-282.

66. Harris, R. A. et al. (2018). A suite of exercises for verifying dynamic earthquake rupture codes. *Seismological Research Letters*, **89**(3), 1146-1162.

67. Roten, D., Olsen, K. B., Day, S. M., & Cui, Y. (2017). Quantification of fault-zone plasticity effects with spontaneous rupture simulations. *Pure and Applied Geophysics*, **174** (9), 3369-3391.

68. Lund, B., and Townend, J. (2007). Calculating horizontal stress orientations with full or partial knowledge of the tectonic stress tensor. *Geophysical Journal International*, **170** (3), 1328-1335.